Biological Modeling of Feathers by Morphogenesis Simulation

Jiajun Zhang and Takashi Kanai
Graduate School of Arts and Sciences
The University of Tokyo, Tokyo, Japan
Email: see https://graphics.c.u-tokyo.ac.jp

***Abstract*—Feathers are sophisticated skin appendages on bird skin, with massive fiber curves (called *barbs*) branching out from a shaft. Each barb uses its hooklets (called *barbules*) to further interlock with each other and form two surfaces. We propose a biological modeling scheme that follows the natural feather development to procedurally reproduce common biological characteristics on outputs. Based on our investigations of biology studies, we chooes to generate pathlines of particles in a velocity field to emulate the helical growth of barb curves inside a cylindrical feather follicle, then apply forward kinematics to pathline curves to mimic the unfurling of a feather after its follicle sheath breaks off. We also develop an optional barb snapping algorithm to mimic the geometric restriction from barbules between barbs. Our modeling scheme can achieve feather growth simulation in 3D rather than 2D space, and it is also the first step to prove that it is feasible to alter macroscopic feather geometry via microscopic barbules, both of these topics are less discussed in the field of CG feather modeling. Because of the high compatibility with biology theories, our scheme is expected to be a better basis for discussing other CG feather topics.**

***Keywords*-Feather; Modeling; Biological; Morphogenesis; Barb; Barbule;**

I. Introduction

Feathers, like hairs and furs, are one of the most noticeable skin appendages that can be found in nature. However, unlike a human hair that can be represented by a single strand, or animal furs that can be rendered in group as offset shells on a surface [1], an individual feather holds a highly complex structure with hierarchical branches, which is insufficient to be described by one simple geometric primitive or pattern.

Simply speaking, a feather has a stiff shaft (called *rachis*) at the middle, to which hundreds of *barbs* attach themselves and adjacently interlock with each other (the hooklets along a barb are called *barbules*) one by one to form two macroscopic-level blades. In order to model such a structure, NURB curves are frequently used to define primary geometric information including rachis, barb curve template, and blade outlines along with various auxiliary parameters in modern CG software. However, artists often need to manually adjust control points to directly approximate feather shapes and patterns. Such an approximation modeling scheme is straightforward, but it does not touch upon the process of real feather growth. Therefore, the morphogenetic factors that may have decisive effects on the final feather shape and pattern cannot be discussed under this scheme.

Outstanding CG techniques originating from the study and measurement of biological materials have been successfully developed with regard to hair rendering [2] in the past. Meanwhile, although few attempts have been made to develop feather modeling techniques by deeply digging biology background, substantial biology researches on feather development are being carried out in recent years. We have also been conducting multidisciplinary investigations on feather morphogenesis to see how we can contribute to areas that cannot be handled with traditional feather modeling schemes.

In this paper, we present a novel modeling scheme that follows the process of feather morphogenesis, abstracts the concepts and phenomena during the development, then maps them into different emulation processes. Our scheme first defines the geometry of a follicle sheath and the growth velocity field to generate barb curves. We then emulate the unfurling process of a feather out of the sheath and adjust barb curves by considering the geometric restrictions of the interlock between them.

II. Related Work

A. Academic studies on feather modeling

The first attempt at modeling CG feathers can be traced back to Dai et al.'s work [3] in 1995. They used user-defined quadratic functions to propagate the orientation of line segments of barb curves in 2D space. However, their work only focused on Galliformes family feathers, and quadratic functions were not sufficient for representing the barb curvature of mature feathers properly.

Chen et al. [4] proposed an impressive method based on parametric L-system grammars. By following pre-defined NURB curve templates, they used the L-system to generate new segments for rachis and barbs, and to limit barb lengths by using two pre-defined NURB curves as outlines.

An important parameterized approach proposed by Streit et al. [5] elaborately defined geometry properties for rachis and barbs. The rachis was modeled by a cubic Bézier curve, and barbs were generated by interpolating multiple key Bézier curves along the rachis. In the same year, Franco et al. [6] independently presented a similar parameterized approach, but unlike the previous one, two Bézier curves

were used as the outline, and the control points of barb Bézier curves were randomly generated.

Recently, Baron et al. [7] proposed a data-driven approach that can produce more biologically sensible outputs. They analyzed real feather atlas and directly extract outline and rachis curve in polynomial or spline form, saving the need for manual definitions. A variant of Franco et al.'s method was then used to generate barb curves.

Some biologists [8][9][10] have attempted to establish mathematical models to describe the barb growth based on feather morphogenesis, but their direct definition of barb angle to rachis has been a drawback. Section III-C shows that the barb angle is dynamic and differs among different stages. Thus their model may be enough for biological discussions but not for CG modeling, Conversely, mature approaches involving the direct definition of barb angles have been used in previous CG works.

B. Industry practices

Based on our review, artists tend to

- use polygon mesh to model large individual feather accompanied by fur for expressing fine details [11],
- directly model barbs as line segments and rely on shading techniques to get high quality [12][13],
- generate barb curves from deformed NURB or polygon surface [14][15].

A number of CG feather modeling tools are based on the variant method from Streit et al. [5] or Franco et al. [6] as it provides sufficient parameters for artists to manually approximate a CG feather geometry to a real feather scanned photo.

III. Biological Background

In this paper, the biological information of a feather is treated as two categories: external *geometric information* and internal *morphogenesis information*. An elaborate explanation about bird feather basis is provided in the early literature from Lucas and Stettenheim [16], while a more modern explanation about feather morphogenesis can be found in the annual review from Chen et al. [17].

A. Feather structure

Feathers are hierarchical branching organs that cover bird skin. At the human-eye recognizable scale, there are three primary components that most of feather types possess:

- *Rachis*: the shaft of a feather,
- *Barbs*: massively branching from two sides of a rachis,
- *Barbules*: massively branching from two sides of a barb.

These components are shown in Figure 1 left. The barbules between two sides of a barb are highly differentiated in some types of feathers. The distal barbules of a barb can hold hooklets that hook the curved margin of the proximal barbules on the adjacent barb, which form a locking state

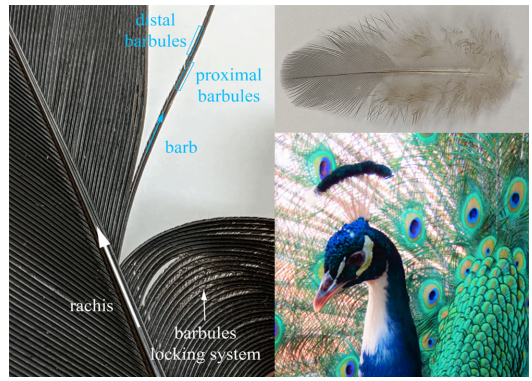

Figure 1. **Left**:Wing feather from Japanese Large-billed Crow. Big white arrow on the rachis shows the direction of the feather tip. Right vane is split manually to exhibit a single barb at the middle and barbules in locking state at the right bottom. Refer to Figure 3 for more details on the anatomical orientation of feathers. **Right-top**: Contour feather from Pigeon, with only partially compact vanes. **Right-bottom**: Tail feathers in background and crest feathers from Peacock head. Take note of the large spacing between barbs that prevents the tail feather from becoming compact. Image by tinkaelectrona is licensed under CC PDM 1.0.

and fasten all barbs together to form one surface at each side: left and right *vanes* [18].

The existence of barbules is one of the key factors that cause diversification of feather type. Figure 1 right-top shows a typical *contour feather*, where the lower barbs hold longer barbules without hooklets so they are fluffy, while the *flight/wing feather* is fully pennaceous so its barbs are highly compact. Moreover, the barb spacing also affects the compactness (Figure 1 right-bottom), since barbules cannot reach each other if the spacing is too large.

B. Feather morphogenesis

Morphogenesis is a biological term used to describe the formation of a certain organ at a cellular level. For feathers, this process takes place inside the cylindrical *follicles* on bird skin [19][17]. When a feather is growing, stem cells (pink squares in Figure 2 A) inside the ring-shaped *collar* actively proliferate and migrate distally. When the proliferated cells reach a thin horizontal area (ramogenic zone in Figure 2 B), they start to differentiate and rearrange, and the wave-like structures, *barb ridges*, start to emerge (Figure 2 C), each of which contains cells for future barb and barbules [20][17]. Therefore, the tip of a feather is actually formed earlier, and we assume that the emergence order and initial location of each barb ridge have a decisive effect on the final tip shape.

How cells are added has a great impact on the final feather shape. Due to the effect of chemical gradients [21][22], barb ridges elongate towards the anterior polarity (Figure 3) after their emergence, causing the helical growth and the fusion of barb ridges into a rachidial ridge (**Ra** in Figure 2 C) that becomes the future rachis. This is the reason why most feathers have such a branching structure. In this case, the first few new barb ridges initially emerge one by one

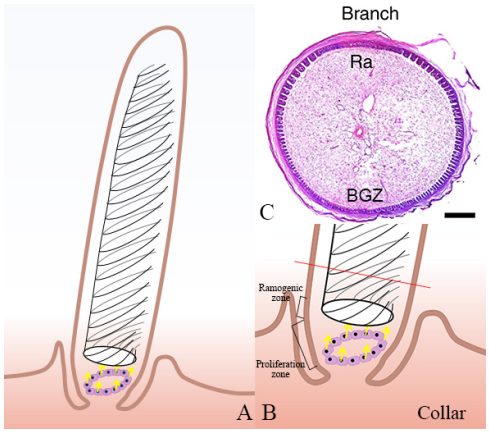

Figure 2. Overview of feather follicle structure. Drawings are based on the findings of Yue et al. [21]. **(A)** Schematic drawing of developing follicle, which shows the helical arrangement of barb ridges (black and gray curves). **(B)** Zoom-in of follicle collar. The proximal ends of barb ridges start to form after cells reach the ramogenic zone. **(C)** Real horizontal cross-section of follicle at level of red line in **B**. **Ra** shows the locus and width of the rachidial ridge at the anterior polarity, the barb ridges lie on the circumference and continuously emerge from the *barb generative zone* **BGZ** located at the posterior polarity. This image **C** by Cheng et al. [23] is licensed under CC BY 4.0. Modified from original.

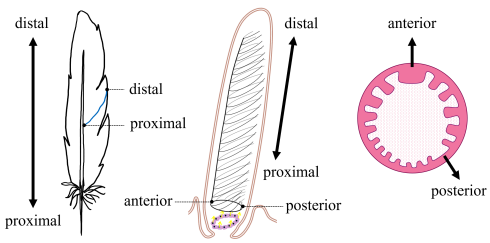

Figure 3. Schematic drawing of anatomical orientation terms.

from anterior towards posterior polarity until the emergence position reaches the *barb generative zone* (**BGZ** in Figure 2 C), where all subsequent new barb ridges emerge from.

C. Feather maturation

When a follicle becomes mature and its sheath starts to break from the distal end, mature barbs and rachis are pushed out, and unfurl themselves from helical to flat forms, similar to how a paper tube is cut and flattened on a table. This break-off process involves the mechanical behavior of barb and barbules, and it creates a particular phenomenon: the "expansion" of two feather vanes [9]. Due to the elasticity of the barb material, each barb may have additional angle changes along its curve, which often causes wider vanes. But due to the locking system, the length and orientation of barbules can restrict this change. However, the details of the underlying mechanical principles remain to be studied.

IV. Method

We propose a biological modeling scheme that procedurally generates feather vanes based on the natural facts

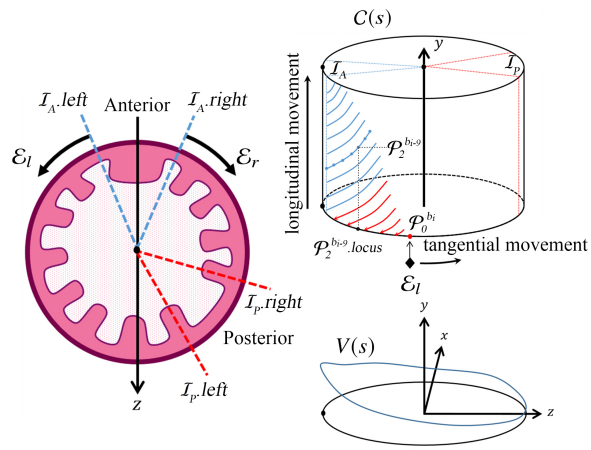

Figure 4. **Left**: Schematic top view of $C(s)$ of follicle cross-section. The arrows indicate the tangential movement direction of $\mathcal{E}_l$ and $\mathcal{E}_r$. **Right-top**: Schematic drawing of $\mathcal{E}_l$ process in helical growth stage. Blue trails indicate the completed barbs. Red trails indicate the developing barbs. **Right-bottom**: Example of speed distribution defined on $C(s)$. Typically, the gradient should slant from the anterior to posterior polarity to match the curvature of the convex tip and barb pattern of the feather.

mentioned in Section III. We first emulate the basic feather morphogenesis and maturation with three stages: Helical growth, Unfurling and Expansion to generate barb curves for two feather vanes, after which the rachis cylinder can be created using an external CG modeling software.

A. Helical growth

The first stage emulates the helical growth of barb ridges inside the follicle, including emergence and elongation, by using the particle movements in a velocity field.

Collar definition: As Figure 4 left shows, we define the collar as a closed curve $C(s)$ parameterized by arc length percentage $s \in [0, 1]$ in right-handed Cartesian space. Mathematical representation (e.g. a circle) or closed composite cubic Bézier curve can be used for this definition.

To simplify the discussion, we use the term *locus* to specify the location s of an object on $C(s)$ in a 1D curvilinear space. We also use the period "." to specify the properties of an object. We assume that the axis of collar is aligned with the $+y$ axis, $C(0)$ is located on the $-z$ axis, and the movement is said to be positive if it follows the clockwise direction. Under these assumptions, a possible definition of collar can be

$$C(s) = \begin{cases} x(s) = \sin(2\pi \cdot s) \\ z(s) = -\cos(2\pi \cdot s) \end{cases} \tag{1}$$

According to Section III-B, we know that the rachidial ridge (anterior polarity) and barb generative zone (posterior polarity) segregate the collar into the left and right arcs. The two polarities of the collar are defined as two intervals $\mathcal{I}_A$ and $\mathcal{I}_P$ on $C(s)$. Specifically, we denote the boundaries of an interval by a locus pair <left, right> (see Figure 4 left).

Additionally, $\mathcal{I}_A$ should be guaranteed to include $C(0)$, $\mathcal{I}_P$ is typically located around $C(0.5)$ but is not mandatory.

Tangential Movement: To generate new barbs, we define two moveable emitters $\mathcal{E}_l$ and $\mathcal{E}_r$ for the left and right side of $C(s)$, so that every emergence of a new barb ridge can be interpreted as an emission from an emitter. As Figure 4 left shows, each emitter starts moving from one boundary of $\mathcal{I}_A$. If all barb ridges are assumed to have the same width denoted by d, after moving $(i+1)\cdot d$, the emitter generates the initial point $\mathcal{P}_0^{b_i}(i = 0, 1, \ldots)$ for the new i-th barb curve b_i. When generated, the current locus of the emitter and current timestamp are recorded to $\mathcal{P}_0^{b_i}.locus$ and $\mathcal{P}_0^{b_i}.t$ respectively. When an emitter meets the same side boundary of $\mathcal{I}_P$, its movement is clamped at the boundary but its emission still proceeds.

Then the tangential speed of emitter movement is determined by its current locus in a steady velocity field defined on $C(s)$. We use $\vec{\boldsymbol{V}}(s)$ to denote any of this kind of field on $C(s)$ and $V(s)$ as its scalar distribution counterpart. Because the directions of emitter movements are already defined (from anterior to posterior polarity), users only need to define its magnitude at each locus in this 1D curvilinear space: a scalar speed distribution $V_e(s)$ for emitters.

The calculation of the trail of a massless particle moving in a velocity field, namely pathline, is a classic problem in fluid mechanics and velocity field visualization [24]: for an arbitrary particle $\boldsymbol{p}$ in any $\vec{\boldsymbol{V}}$ at time t, it must satisfy:

$$\frac{d\boldsymbol{p}}{dt} = \vec{\boldsymbol{V}}(\boldsymbol{p}(t)) \tag{2}$$

Therefore, the pathline can be calculated by integrating Equation 2, and the locus of emitters can be calculated as

$$\mathcal{E}_l.locus = \max\left\{\mathcal{I}_P.left, \mathcal{I}_A.left - \int_{\mathcal{P}_0^{b_i}.t}^{t_{curr}} V_e(s(t))dt\right\} \tag{3}$$

$$\mathcal{E}_r.locus = \min\left\{\mathcal{I}_P.right, \mathcal{I}_A.right + \int_{\mathcal{P}_0^{b_i}.t}^{t_{curr}} V_e(s(t))dt\right\} \tag{4}$$

where t_{curr} refers to the global timestamp after the emulation starts from 0 second. The 4th-order Runge-Kutta method is used as the solver in our implementation.

To emulate barb elongation, once $\mathcal{P}_0^{b_i}$ is generated, it starts moving like an emitter, but in the opposite direction on $C(s)$. After every iteration of numerical calculation, the locus of $\mathcal{P}_0^{b_i}$ is recorded as subsequent points $\mathcal{P}_j^{b_i}(j = 1, \ldots)$ for the barb b_i. The tangential speed is defined as a speed distribution $V_b(s)$ for all barbs. When $\mathcal{P}_0^{b_i}$ meets the boundary of $\mathcal{I}_A$, the elongation terminates and b_i is considered as completed and mature (blue trails in Figure 4 right-top). Equation (3) (4) can also be applied to the calculation of $\mathcal{P}_j^{b_i}.locus$ by replacing each term correspondingly.

Longitudinal Movement: New cells migrate upward from bottom and push old cells higher, we emulate this activity as longitudinal movement aligned to the y axis. The scalar growing speed v_{grow} of the follicle defined by the user is used for calculating the y coordinate of $\mathcal{P}_j^{b_i}$:

$$\mathcal{P}_j^{b_i}.\boldsymbol{p}.y = v_{grow} \cdot (t_{curr} - \mathcal{P}_j^{b_i}.t) \tag{5}$$

where $\mathcal{P}_j^{b_i}.\boldsymbol{p}$ refers to the 3D world space position of $\mathcal{P}_j^{b_i}$.

Termination & Conversion: The emulation can be terminated when N barbs of either vane are mature, and all other developing barbs (red trails in Figure 4 right-top) are discarded. The x and z coordinate of $\mathcal{P}_j^{b_i}.\boldsymbol{p}$ are calculated by simply evaluating $C(s)$ by $\mathcal{P}_j^{b_i}.locus$. In order to reduce the high density of generated barb curve points, we introduce a downsampling process by only selecting every f-th point for the output, with most proximal and distal points always included. After all barb curve points are converted into 3D space vertices, the result is delivered to the next stage.

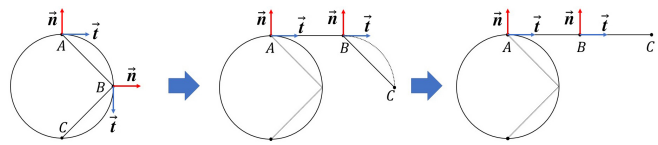

Figure 5. Schematic top view of effect of partial unfurling and fully unfurling. The collar is represented by circle and the line sequence $\overline{ABC}$ is a barb curve downsampled to 3 vertices. Vertex A is the root of this discrete curve. Tangent is continuous at vertex B when partially unfurled.

B. Unfurling

The second stage emulates the flattening of feather vanes released from the follicle sheath by using forward kinematics. Although the barb growth direction is from distal to proximal, from a forward kinematics perspective, a proximal vertex is the parent of its distal vertex child. For simplifying the discussion, from now on, $\mathcal{P}_j^{b_i}(j = 0, 1, \ldots)$ denote barb vertices from the proximal to distal end.

Selection of frame: A 3D space discrete curve is defined by a finite sequence of 3D space vertices on an original smooth curve, and our output from the last stage can be seen as discrete curves. At each vertex $\mathcal{P}_j^{b_i}$, there is a discrete frame consisting of three unit vectors: tangent $\vec{\boldsymbol{t}}$, normal $\vec{\boldsymbol{n}}$ and binormal $\vec{\boldsymbol{b}}$. We calculate this frame as:

$$\mathcal{P}_j^{b_i}.\vec{\boldsymbol{t}} = dir \cdot \frac{dC(\mathcal{P}_j^{b_i}.locus)}{ds} \tag{6}$$

$$\mathcal{P}_j^{b_i}.\vec{\boldsymbol{n}} = \mathcal{P}_j^{b_i}.\vec{\boldsymbol{b}} \times \mathcal{P}_j^{b_i}.\vec{\boldsymbol{t}} \tag{7}$$

$$\mathcal{P}_j^{b_i}.\vec{\boldsymbol{b}} = \vec{\boldsymbol{u}}_y \tag{8}$$

where $\vec{\boldsymbol{u}}_y$ is a unit vector of y axis, $dir = -1$ for left vane and $dir = 1$ for right vane. Note that our discrete frame is different from the discrete frenet frame. The latter uses $\vec{\boldsymbol{t}}$ to indicate elongation direction of a curve, while ours indicates only the tangential movement direction of helical growth.

Figure 5 shows an example of unfurling a barb. We assume the binormal at each vertex to be the rotation axis. Unfurling can be achieved by aligning

1) each line segment to the tangent of the parent frame,
2) each tangent to the tangent of the parent frame,

and it ensures similar tangent continuity between discrete curve $\overline{ABC}$ and virtual arc $\widehat{ABC}$ when only a part of barb curves are fully unfurled.

Hierarchization & Rotation: The execution of unfurling involves rotation but it requires a hierarchical chain for each barb curve. Discrete frames can help build such hierarchy by using its normalized vectors as orthonormal coordinate basis. For $\mathcal{P}_{j+1}^{b_i}$, we can calculate all vector porperties (position, discrete frame, etc.) of the hierarchized vertex $\hat{\mathcal{P}}_{j+1}^{b_i}$ located in the local space formed by the frame of parent $\hat{\mathcal{P}}_{j}^{b_i}$ as

$$\hat{\mathcal{P}}_{j+1}^{b_i} = \mathbf{M}_j^{b_i} \mathcal{P}_{j+1}^{b_i}, \qquad \hat{\mathcal{P}}_0^{b_i} = \mathcal{P}_0^{b_i} \tag{9}$$

where the transformation matrix $\mathbf{M}_j^{b_i}$ can be written as

$$\mathbf{M}_j^{b_i} = \hat{\mathbf{M}}_{j-1}^{b_i} \cdots \hat{\mathbf{M}}_0^{b_i}, \qquad \hat{\mathbf{M}}_j^{b_i} = \left(\hat{\mathbf{R}}_j^{b_i}\right)^{-1} \left(\hat{\mathbf{T}}_j^{b_i}\right)^{-1} \tag{10}$$

where the rotation matrix $\hat{\mathbf{R}}_j^{b_i}$ is built by $\hat{\mathcal{P}}_j^{b_i}.\vec{\boldsymbol{t}}$, $\hat{\mathcal{P}}_j^{b_i}.\vec{\boldsymbol{n}}$ and $\hat{\mathcal{P}}_j^{b_i}.\vec{\boldsymbol{b}}$, and the translate matrix $\hat{\mathbf{T}}_j^{b_i}$ is built by $\hat{\mathcal{P}}_j^{b_i}.\boldsymbol{p}$.

After hierarchization, the tangent and binormal are always $\vec{\boldsymbol{u}}_z = (0,0,1)$ and $\vec{\boldsymbol{u}}_y = (0,1,0)$ for each parent frame, so the alignment of $\overrightarrow{\mathcal{P}_{j-1}^{b_i}\mathcal{P}_j^{b_i}}$ and $\mathcal{P}_j^{b_i}.\vec{\boldsymbol{t}}$ to $\mathcal{P}_{j-1}^{b_i}.\vec{\boldsymbol{t}}$ can be done by simple linear algebra. If we apply a weight $w \in [0,1]$ to the rotation angle, we can further control the degree of unfurling.

C. Expansion

The third stage emulates the additional barb curve change based on the restriction from barbules. Due to the lack of biological supports and mechanical analysis, it is beyond our capabilities to correctly reproduce this phenomenon. However, the geometric restriction from barbules can still be considered.

Construction of barbules: Barbules grow inside barb ridge, and the shaft they fuse to has a special term *ramus*. After a barb ridge matures, the enclosed barbules are released and rotate around the ramus to flatten themselves. Because the tangential and longitudinal movement velocity of helical growth depict the ideal elongation direction at each vertex, we can calculate the ramus vector $\vec{\boldsymbol{r}}$ at $\mathcal{P}_j^{b_i}$ as

$$\vec{\boldsymbol{r}} = v_{grow} \cdot \mathcal{P}_j^{b_i}.\vec{\boldsymbol{b}} + V_e(\mathcal{P}_j^{b_i}.locus) \cdot \mathcal{P}_j^{b_i}.\vec{\boldsymbol{t}} \tag{11}$$

See Figure 6 top-right for details.

After finding the ramus vector, we can construct two barbules in the semi-spherical coordinate system (Figure 6 bottom-right). We assume that the ramus is located at the crest of the barb ridge, and the same angle is flattened for the two barbules. So if a barb ridge has l_{ridge} height, the distal barbule vector $\vec{\boldsymbol{v}}_d$ can be calculated as (substituting θ_d to θ_p to calculate proximal barbule vector $\vec{\boldsymbol{v}}_b$)

$$\vec{\boldsymbol{v}}_d = \mathbf{R}(\vec{\boldsymbol{r}}, \phi) \left(\frac{l_{ridge}}{\tan(\theta_d)} \cdot \frac{\vec{\boldsymbol{r}}}{|\vec{\boldsymbol{r}}|} + dir \cdot l_{ridge} \cdot \mathcal{P}_j^{b_i}.\vec{\boldsymbol{n}} \right) \tag{12}$$

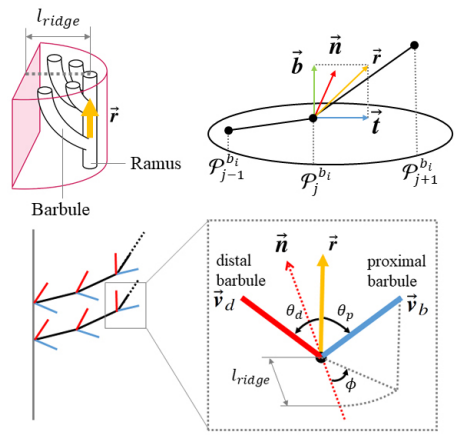

Figure 6. **Top-Left**: Schematic drawing of internal structure of barb ridge. **Top-Right**: Schematic drawing of calculating ramus vector $\vec{\boldsymbol{r}}$ (yellow arrow). $\vec{\boldsymbol{r}}$ is lying on the plane formed by $\vec{\boldsymbol{t}}$ and $\vec{\boldsymbol{b}}$. **Bottom-Left**: Schematic drawing of mature barb with barbules. **Bottom-Right**: Schematic drawing of release of barbules from barb ridge. ϕ: Azimuth rotation angle for two barbules, $\phi = \pi/2$ in this case. θ_d&θ_p: Zenith angle from ramus to distal/proximal barbule.

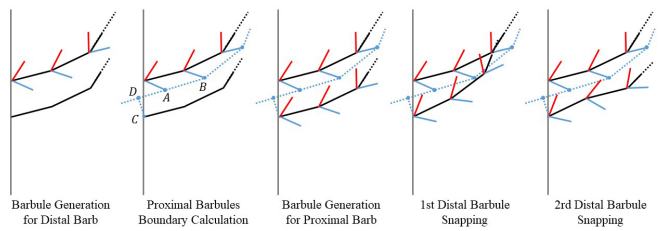

Figure 7. Schematic drawing of snapping between two adjacent barbs. Gray vertical line indicates one side of the rachis.

where *dir* is the same as the one in Equation 6. The zenith angle θ_d (or θ_p) and the azimuth angle ϕ for constructing rotation matrix $\mathbf{R}(\vec{\boldsymbol{r}}, \phi)$ around $\vec{\boldsymbol{r}}$ are all defined by the user.

Snapping of barbules: If vanes hold barbules that are fully interlocked with each other, each barb must fully snap to the adjacent one. Based on this geometric restriction, we propose an algorithm to snap two barbs by rotating the discrete frame at every barb curve vertex. Because only distal barbules have hooklets, the snapping should start from the most distal barb and proceed proximally. One cycle of our algorithm can be summarized as follows (Figure 7):

1) Generate proximal barbules for the current barb from the proximal to distal end.
2) Calculate the boundary formed by the tips of proximal barbules.
3) Generate distal barbules for the next barb from the proximal to distal end.
4) For each vertex, rotate its frame so that the tip of its distal barbule touches the boundary above. If they cannot be touched, stop processing all subsequent vertices.

When constructing the boundary, there is a gap between

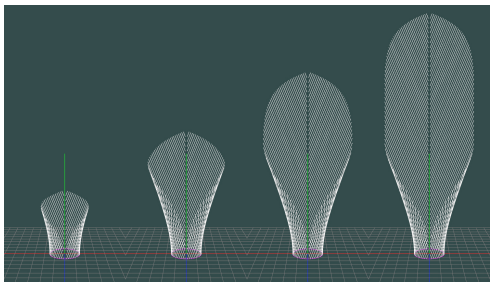

Figure 8. Generation sequence of contour feather with helical growth stage and unfurling stage enabled. The global timestamps t_{curr} for each image from left to right are 6 sec, 12 sec, 18 sec, and 24 sec.

the rachis and the first proximal barbule. As Figure 7 shows, the first line segment of the boundary $\overline{AB}$ is extended to cover this gap, then the root vertex C of the next barb projects itself to $\overline{AB}$ as D to form a new line segment.

After constructing the boundary from b_i, for $\mathcal{P}_j^{b_{i+1}}$ on b_{i+1}, we check the intersection of two elements:

- sphere with $\mathcal{P}_j^{b_{i+1}}$ as center and $|\mathcal{P}_j^{b_{i+1}}.\vec{v}_d|$ as radius,
- each line segment that forms the boundary.

If the intersection exists, we always take the most distal intersection position then snap the tip of current distal barbule to this position.

V. Results and Discussion

Implementation: Our program is implemented by C++ and OpenGL, and runs on a desktop PC with Intel® Xeon™ E3 3.30GHz CPU and NVIDIA® GeForce GTX 760 GPU and 16GB RAM. The real-time procedural generation of feather vanes can be performed at 30 ~ 60 fps, allowing the interactive adjustment for artists. As for the parameter configuration in our program, we use a similar definition like Equation 1 for $C(s)$. For any scalar distribution/gradient on $C(s)$, we use curve editor for its definition.

Considering the particularity of our theme and the close relationship with biology, our primary evaluation method is to check whether we have the ability to reproduce common biological characteristics, and also to compare the characteristics between our outputs and real feathers.

Growth simulation: Figure 8 shows a typical result of our implementation. The helical stage is responsible for continuously pushing new barbs out, resulting in two vanes growing from the base. With the unfurling stage enabled and the global unfurling factor w set to 1.0, all helical barbs are fully unfurled, presenting a realistic simulation of feather breaking out from follicle sheath in 3D space.

Tip, lateral side, and bottom shape: Due to the mechanism of morphogenesis explained in Section III-B, the determinants for the different parts of the vane outline are different. The curvature of the tip shape highly relies on the different emergence timestamp of each barb ridge, resulting in height offset among the distal end of barbs, and

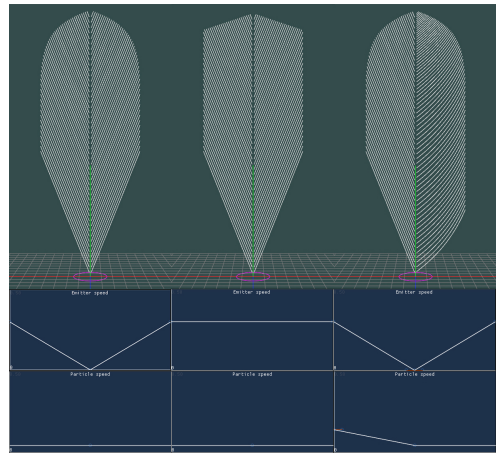

Figure 9. Different vane outlines under different speed distributions.

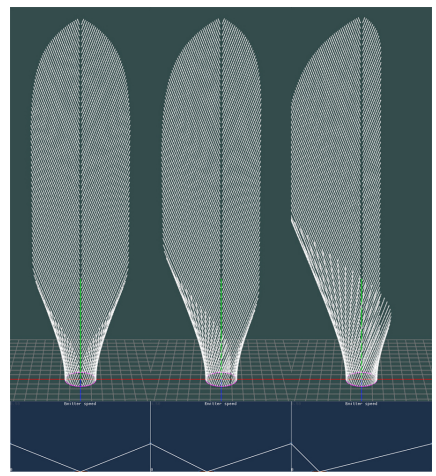

Figure 10. Feather vane asymmetry controlled by the locus shifting of the posterior polarity. The posterior polarity intervals $\mathcal{I}_P$ from left to right are $\mathcal{I}_P.left = 0.51$, $\mathcal{I}_P.right = 0.49$; $\mathcal{I}_P.left = 0.41$, $\mathcal{I}_P.right = 0.39$; $\mathcal{I}_P.left = 0.21$, $\mathcal{I}_P.right = 0.19$.

is controlled by $V_e(s)$ (Figure 9 left). The $V_e(s)$ is convex downward at $s = 0.5$ so that the speed of emitters slows down when approaching BGZ, making the tip slopes blend perfectly into the two lateral sides of vanes.

Figure 9 middle is an extreme case of the tip shape not blending into the lateral sides but forming two distinct sharp angles that look abnormal. This phenomenon exists in nature and can be found on specific birds. A good example is the tail feather of Wild Turkey.

$V_b(s)$ controls the barb patterns, which also means it can control the bottom shape of feather vanes, because the bottom shape is just the curve of the most proximal barb itself for many compact feathers (Figure 9 right).

Vane asymmetry: The different arc lengths on the collar from the anterior to posterior polarity is the reason why some feathers may have asymmetric vanes, and it is a critical biological characteristic for the aerodynamics of flight/wing

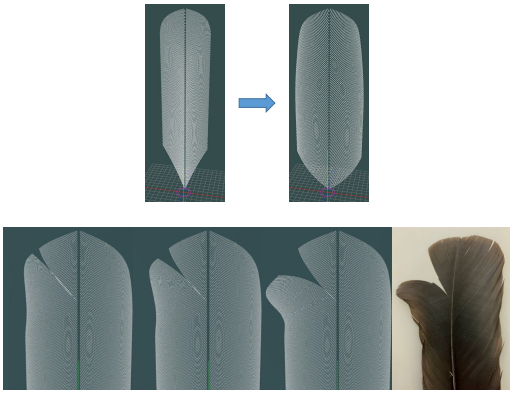

Figure 11. Feather without expansion (top-left) and with expansion (top-right). Vane splitting compared with real feather (bottom-row).

feathers. Figure 10 shows how the vane width asymmetry is controlled by only moving the interval of $\mathcal{I}_P$ (posterior polarity) from about $s = 0.5$ to $s = 0.2$ on $C(s)$. The change of the tip slope and vane width correctly reflects the characteristic of asymmetric wing feather that the nearer a wing feather is located to the end of a wing, the narrower is its distal vane (leading edge), and the broader is its proximal vane (trailing edge) [16].

Expansion: Although expansion is one of the most difficult phenomena to simulate due to its mechanical complexity, our geometric-restriction based algorithm indeed boosts the reality of the outputs. There is a common characteristic for compact vanes that during the morphogenesis the barb ridges near the posterior polarity are usually smaller than those near the anterior polarity. This often causes the barbule length to decrease distally. As a result, the barb spacings around the edge of vanes appear more compact than those around the rachis. The measurement data from Feo et al. [10] also proves this characteristic. So we give a similar distribution for barb ridge height l_{ridge} and assign it as a property to $\mathcal{P}_j^{b_i}$ based on $\mathcal{P}_j^{b_i}.locus$. The result is the same as we expect (Figure 11) when valid parameters are used. Furthermore, our snapping algorithm allows calculation of the vane deformation when it is split. By manually bending an intermediate barb curve before executing snapping algorithm, the vane can be split and lower barbs can be deformed accordingly.

However, we found that our algorithm suffers a flaw caused by the insufficient barbule information at the proximal end of a barb. In Figure 12, we have to extend the line segment AB of the proximal barbules boundary to cover the barbule-absent area. However, the extension of AB cannot always guarantee the intersection with the sphere with center C and radius $|\overrightarrow{CD}|$. As a result, the snapping process for this whole barb is skipped, and the valid range of parameter settings is limited.

On the other hand, the phenomenon in the left of Figure 12

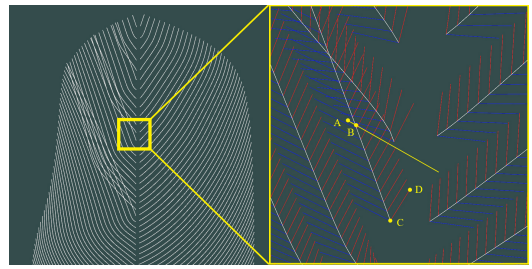

Figure 12. A flaw occurred in expansion. Certain barbs cannot snap to their adjacent distal barbs because of the inappropriate boundary extension. Proximal barbules are in blue. Distal barbules are in red.

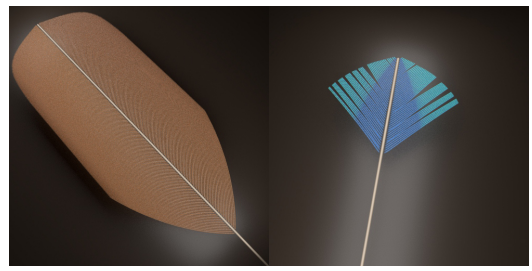

Figure 13. Rendered wing and crest feather by using our output in Maya.

indeed exists in nature, it can be interpreted as the barbules are intentionally unzipped at these places. It is common to find this kind of flaw on real feathers but the reason causing this flaw in our output is not desired.

Figure 13 shows the rendered feathers using our output. All of the three stages are used to produce the feather vanes. Barb curves are rendered as ribbons, and rachis is modeled by a simple cylinder in CG software. Note that the crest feather at the right is modeled by stopping the whole emulation process before emitters reach the barb generative zone, leading to the generation of tip barbs only.

VI. Conclusion and Future Work

In this paper, we present a novel feather modeling scheme by referring to existing studies on microscopic biological activities inside feather follicle and emulating the real growth of a feather.

In our scheme, the helical growth stage generates a prototype of two vanes in a unified model, avoiding the independent definition of the geometry of two vanes without taking biological correlations into consideration. The usage of collar also guarantees the blendability of different vane asymmetry by simply moving the locus of posterior polarity.

The unfurling stage emulates the "hatching" of a feather from its follicle sheath, which provides the possibility to animate the growth process of a feather.

The expansion stage emulates the geometric restriction from barbules, and provides a feasible way to express the microscopic level influence on the macroscopic level shape.

In summary, the most important advantage of our scheme is the linkage to biological studies, meaning that it has the

potential to transplant cellular mechanism to CG feather modeling to internally guarantee biologically-sensible output, and users are not required relevant biology knowledge to manually ensure this. We take the first step to study the relationship between barbules length and feather vane shape & barb pattern, which has not been discussed yet in the field of CG feather modeling. Our work can also be a basis of visual characteristics rendering from barbules like structural color, which has a high correlation with barbule orientation (our modeling scheme can conveniently provided this information). However, our advantage is also our limitation. Many biology theories are qualitative rather than quantitative, and the valid ranges of parameters are limited.

In the future, we aim to further improve our scheme. In this study, we assumed that all barb ridges have the same width in the helical growth stage, which is not true from a biological perspective. "How barb ridge width affects the curvature of final barbs and collar size" is still unknown and needs investigation. In addition, since the collar changes size during the different phases in regenerative cycling, we are considering to explore its influence on the lateral side shape of feather. Finally, it is promising to develop a more precise barb snapping algorithm by investigating barb and barbule properties in the bioengineering field.

References

[1] J. Lengyel, E. Praun, A. Finkelstein, and H. Hoppe, "Real-time fur over arbitrary surfaces," in *Proc. Symposium on Interactive 3D Graphics*. ACM, 2001, pp. 227–232.

[2] S. R. Marschner, H. W. Jensen, M. Cammarano, S. Worley, and P. Hanrahan, "Light scattering from human hair fibers," in *ACM SIGGRAPH 2003 Papers*. ACM, 2003, pp. 780–791.

[3] W.-K. Dai, Z.-C. Shih, and R.-C. Chang, "Synthesizing feather textures in galliformes," *Comput. Graph. Forum*, vol. 14, no. 3, pp. 407–420, 1995.

[4] Y. Chen, Y. Xu, B. Guo, and H.-Y. Shum, "Modeling and rendering of realistic feathers," *ACM Trans. Graph.*, vol. 21, no. 3, pp. 630–636, Jul. 2002.

[5] L. Streit and W. Heidrich, "A biologically-parameterized feather model," *Computer Graphics Forum*, vol. 21, no. 3, pp. 565–573, 2003.

[6] C. G. Franco and M. Walter, "Modeling and rendering of individual feathers," in *Proc. XV Brazilian Symposium on Computer Graphics and Image Processing*. IEEE Comput. Soc, 2002, pp. 293–299.

[7] J. Baron and E. Patterson, "Procedurally generating biologically driven feathers," in *CGI2019: Advances in Computer Graphics*, vol. 11542. Springer International Publishing, 2019, pp. 342–348.

[8] R. O. Prum and S. Williamson, "Theory of the growth and evolution of feather shape," *Journal of Experimental Zoology*, vol. 291, no. 1, pp. 30–57, 2001.

[9] T. J. Feo and R. O. Prum, "Theoretical morphology and development of flight feather vane asymmetry with experimental tests in parrots," *Journal of Experimental Zoology Part B: Molecular and Developmental Evolution*, vol. 322, no. 4, pp. 240–255, 2014.

[10] T. J. Feo, E. Simon, and R. O. Prum, "Theory of the development of curved barbs and their effects on feather morphology: Theoretical morphology of curved feather barbs," *Journal of Morphology*, vol. 277, no. 8, pp. 995–1013, 2016.

[11] D. Kaufman, "STUART LITTLE 2: Let the feathers fly," in *ACM SIGGRAPH 2002 Courses*. ACM, 2002.

[12] T. Rzankowski, "SideFX intern program - feather tools," 2017, houdini Hive at SIGGRAPH 2017.

[13] B. Levin, "Creating PIPER: Pixar's latest short film," in *ACM SIGGRAPH 2016 Talks*. ACM, 2016.

[14] D. Seddon, M. Auflinger, and D. Mellor, "Rendertime procedural feathers through blended guide meshes," in *ACM SIGGRAPH 2008 Talks*. ACM, 2008, pp. 76:1–76:1.

[15] Jeepster. (2015) Bioluminescent macaw. [Online]. Available: https://blenderartists.org/t/bioluminescent-macaw/638164

[16] A. M. Lucas and P. R. Stettenheim, *Avian anatomy : integument*. U.S. Goverment Printing Office, 1972.

[17] C.-F. Chen, J. Foley, P.-C. Tang, A. Li, T. X. Jiang, P. Wu, R. B. Widelitz, and C. M. Chuong, "Development, regeneration, and evolution of feathers," *Annual Review of Animal Biosciences*, vol. 3, no. 1, pp. 169–195, 2015.

[18] F. Zhang, L. Jiang, and S. Wang, "Repairable cascaded slide-lock system endows bird feathers with tear-resistance and superdurability," *Proceedings of the National Academy of Sciences*, vol. 115, no. 40, pp. 10 046–10 051, 2018.

[19] M. Yu, Z. Yue, P. Wu, D.-Y. Wu, J.-A. Mayer, M. Medina, R. B. Widelitz, T.-X. Jiang, and C.-M. Chuong, "The developmental biology of feather follicles," *The International journal of developmental biology*, vol. 48, no. 0, pp. 181–191, 2004.

[20] M. Yu, P. Wu, R. B. Widelitz, and C.-M. Chuong, "The morphogenesis of feathers," *Nature*, vol. 420, p. 308, 2002.

[21] Z. Yue, T.-X. Jiang, R. B. Widelitz, and C.-M. Chuong, "Wnt3a gradient converts radial to bilateral feather symmetry via topological arrangement of epithelia," *Proc. National Academy of Sciences*, vol. 103, no. 4, pp. 951–955, 2006.

[22] J. Lin and Z. Yue, "Coupling of apical-basal polarity and planar cell polarity to interpret the wnt signaling gradient in feather development," *Development*, vol. 145, no. 17, 2018.

[23] D. Cheng, X. Yan, G. Qiu, J. Zhang, H. Wang, T. Feng, Y. Tian, H. Xu, M. Wang, W. He, P. Wu, R. B. Widelitz, C.-M. Chuong, and Z. Yue, "Contraction of basal filopodia controls periodic feather branching via notch and FGF signaling," *Nature Communications*, vol. 9, no. 1, pp. 1–11, 2018.

[24] D. Kao, "Introduction to vector field visualization," in *Proc. IEEE Pacific Visualization Symposium, Tutorial*, 2010.